# Factors Contributing to Heat Affected Zone Damage in Grade 91 Steel Feature Type Cross-weld Tests

**John A. Siefert[1], Dr. Jonathan D. Parker[2] and Rachel C. Thomson[3]**
[1]PhD Student at Loughborough University and Electric Power Research Institute, North Carolina, USA
[2]Electric Power Research Institute, North Carolina, USA
[3]Department of Materials, Loughborough University, Leicestershire, LE11 3TU, UK

**John A. Siefert, Electric Power Research Institute, jsiefert@epri.com**

## Summary
Grade 91 steel has been widely utilized in power plants over the last 20 years. Its specification worldwide has dramatically increased since the acceptance of ASME Code Case 1943 for this material in 1983. Recent evaluation of a combination of ex-service Grade 91 steel components and virgin material has provided a unique opportunity to revisit commonly stated factors which contribute to damage in cross-weld creep tests. The approach adopted here is grounded in the fundamental objective of linking metallurgical risk factors in Grade 91 steel to the cross-weld creep performance. Establishing metallurgical risk factors in 9%Cr steels is regarded as a key consideration in the integration of a well-engineered life management strategy for these complex materials.

In this study, two heats of ex-service Grade 91 steel which exhibit a similar response to the deformation resistance (i.e. strength) but dramatic differences in the susceptibility to damage (i.e. creep ductility) were evaluated in the welded condition using large, feature type cross-weld creep samples. Heat affected zone damage was investigated from both a macro-damage and micro-damage perspective. The macro-damage evaluation provided a comprehensive understanding of the global damage distribution through the heat affected zone (HAZ). The damage was linked to extensive hardness mapping and calculated peak temperatures through the HAZ. The micro-damage characterization included a number of local observations for cavities in each sample using scanning electron microscope techniques. General observations were made regarding the shape and size of creep cavities and association of damage with microstructural features. These observations were linked to the as-fabricated microstructure and as characterized by electron backscatter diffraction (EBSD) and energy dispersive x-ray spectroscopy (EDS) mapping.

## Key Words
Grade 91
Heat Affected Zone
Damage
Cross-weld
Creep

## Introduction
The life management of 9%Cr creep strength enhanced ferritic (CSEF) steels is emerging as a vital focused research area for fossil fired power plants as components constructed from Grade 91 and Grade 92 steel have demonstrated wide variability in performance [1-5]. Factors which affect performance can be generally classified into four key areas: design, fabrication/construction, operation and metallurgy. State-of-the-art power plants and for both conventional pulverized coal and heat recovery steam generators (HRSGs) are now commonly designed with a main steam and hot reheat temperature ≥600°C. This reality is driving an ever-more-important need to better understand the key factors which affect long-term performance and revisit commonly held beliefs regarding component performance.

There is an increasing need to fully appreciate the factors which affect deformation and damage as the service experience until the early 2000s was predicated on plant applications that only operated in steam outlet temperatures to ~550°C, **Error! Reference source not found.** [6]. Furthermore, and as stated from a manuscript in the year 2004 [7], "*Although components made of X10CrMoVNb9-1 (P91) installed in Germany show a service time of over 80,000h [installation in ~1994 or prior], few experiences with creep damages under service conditions exist. Among other reasons this is due to the very moderate loading conditions of first projects (e.g. P91 in power plant Tiefstack, 1992, steam parameters 540°C/240 bar).*" This is an important set of observations as plant components operating <550°C (with the exception of dissimilar metal welds) are less susceptible to creep dominated failures by the reality that the operating temperature is comparatively low to the recognized creep regime for this class of materials. This is in sharp

contrast to recent publications which have detailed extensive damage in headers operating in the UK at temperatures >565°C [3-5].

| Plant | Country | MWe | SH* Steam (°C, °F) | RH** Steam (°C, °F) | Year Commissioned |
|---|---|---|---|---|---|
| Milmerran 1 & 2 | Australia | 400 | 568, 1054 | 596, 1105 | 2002 |
| Sidi Krir 3 & 4 | Egypt | 340 | 540, 1006 | 540, 1004 | 2002 |
| Hawthorn 5 | USA | 550 | 540, 1005 | 540, 1005 | 2001 |
| Rutenberg B 3 & 4 | Israel | 550 | 540, 1006 | 540, 1006 | 2000 |
| Saba | Pakistan | 138 | 540, 1005 | 538, 1001 | 1999 |
| Nantong 3 & 4 | China | 350 | 540, 1005 | 540, 1005 | 1999 |
| Yangzhou 1 & 2 | China | 600 | 540, 1006 | 539, 1002 | 1999 |
| Taichung 5, 6, 7 & 8 | Taiwan | 550 | 542, 1008 | 542, 1008 | 1996 |

*Table 1: Application of Grade 91 Steel from One Original Equipment Manufacturer (OEM) per a Conference Paper from 2001 [6]*
**SH = Superheater steam temperature*
***RH = Reheater steam temperature*

Historically, the performance of complex structures operating in the creep regime was recognized as being controlled by both deformation and damage. In particular, and although it is well established that the heat affected zone (HAZ) in Grade 91 and 92 steels is much weaker in cross-weld performance (a so-called weld strength reduction factor or WRSF), the contribution of damage susceptibility to performance has not been well appreciated or defined. The focus in prior and recent publications continues to be to establish a rationale for performance on the basis of microstructural features which affect deformation.

Due to the difficulties associated with managing power plant assets, and 9%Cr steels in particular, by non-destructive evaluation alone there has been a renewed interest of risk-ranking components in a given utility fleet or a particular plant [8. 9]. As the performance of welded components subjected to multiaxial stress states will likely be life-limiting to many critical components in the plant, it is vital to link the parent metal condition and composition to the cross-weld creep performance and for a set of well-controlled, relevant test conditions. To address this objective, the results provided in this manuscript attempt to link key observations in the parent metal composition and inclusion content to the evolution of damage in a feature, cross-weld creep test geometry that is sufficiently large to result in a multiaxial stress state in the gauge section. The methods employed include a variety of common techniques which attempt to characterize the damage in the post-test condition to the initial, as-fabricated state using both macro- and micro-based techniques.

## Experimental Procedure

### *Selection of Parent Materials, Chemical Composition and Inclusion Analysis*

The following analysis techniques, and as validated in a recent round robin study led by the International Institute of Welding were utilized to determine the composition of each of the elements [10].

1. Inductively coupled plasma optical emission spectrometry (ICP-OES) ➔ Al, B, Ca, Co, Cr, Cu, La, Mn, Mo, Nb, Ni, P, Si, Ta, Ti, V, W, Zr
2. Inductively coupled plasma mass spectrometry (ICP-MS) ➔ As, Bi, Pb, Sb, Sn
3. Combustion ➔ C, S
4. Insert gas fusion (IGF) ➔ O, N

Inclusion analysis was conducted using an automated scanning electron microscope coupled with energy dispersive spectroscopy (SEM-EDS) using a tungsten source. The system used was FEI's Aspex Explorer model. Analysis was performed using the Automated Feature Analysis (AFA) and reports created using the Metals Quality Analysis (MQA) software. The following parameters were utilized: accelerating voltage of 20 KeV, a working distance of ~17 mm, a minimum EDS scan time of 1 second, a maximum EDS scan time of 2 seconds and in an area measuring 7.2 X 7.2 mm (51.5 $mm^2$). The minimum identified particle threshold was set to 1 µm and the maximum to 228 µm in diameter.

### *Welding and Weld Thermal Cycle Analysis*

Material for this evaluation was sourced from an ex-service superheater outlet header which operated in a supercritical power plant in the UK for ~80,000 hours at ~570°C [4]. Two heats of material were selected with known, significant differences in creep ductility. The material with poor creep ductility, B2, was re-normalized and tempered at 1065°C/0.5h/AC + 765°C/2h/AC to produce a deformation resistance similar to that of the material with better

creep ductility, TP1. The re-heat treated B2 (e.g. identified as 'RNT-B2') and TP1 were tested in uniaxial creep to evaluate the pre-weld condition at 625°C and 100 MPa. In these tests, the RNT-B2 achieved a life of 3,360 hours and a reduction of area of 15%. Similarly the TP1 test achieved a life of 2,950 hours but exhibited a much higher reduction of area, 83%.

Weldments were fabricated in a machined U-groove excavation (15° bevel) in each heat of material using best practice guidance for the shielded metal arc welding (SMAW) process as detailed in [11] including a minimum preheat temperature of 150°C (300°F), a maximum interpass temperature of 315°C (600°F), stringer beads and removal of slag after each weld layer through light grinding. Following welding each weldment was given a post weld heat treatment (PWHT) at 675°C for 2 hours. The applied PWHT was selected as part of an initiative to reduce the minimum required PWHT temperature in ASME B&PV Code Section I, Table PW39-5. At the time of fabrication of the weldments detailed in this manuscript, the minimum required PWHT was 730°C (1350°F), more recently this value has been reduced for thin wall components (e.g. <13 mm) to 675°C (1250°F) and for thick wall components to 705°C (1300°F). This effort was driven, in large part, due to concerns regarding field PWHT of thick-section and complex components.

Solutions for thick-plate thermal heat flow have been investigated and evolved since Rosenthal introduced his solutions in the early 1940s. Simplified examples exist for an approximate determination of the calculated peak temperature in the HAZ and with respect to the fusion line using a range of potential solutions. The selected solution is provided as an example problem in [12] for a 3D thick plate solution and the required variables to calculate the temperature distribution are given in Table 2.

| Sample | Interpass Temp. | Amperage | Voltage | Travel Speed | Arc Efficiency | Thermal Diffusivity | Melting Temp. | Enthalpy Increment |
|---|---|---|---|---|---|---|---|---|
| **Units** | **°C** | **A** | **V** | **mm/s** | **N/A** | **$mm^2/s$** | **°C** | **$J/mm^3$** |
| 7C | 205 | 115 | 23.3 | 2.34 | 0.75 | 6.1 | 1500 | 7.5 |
| RNT-B2 | 178 | 122 | 24.0 | 2.96 | | | | |

*Table 2: Welding Parameters and Variables Required to Solve the Heat Flow Equations in [12]*

***Hardness Mapping***

Each weldment was characterized after welding and PWHT by hardness mapping. The equipment utilized for the hardness mapping characterization was a LECO Automatic Hardness Tester, Model AMH-43. Hardness mapping was conducted so that the requirements in both ASTM E384-11 and ISO 6507 were met. The dimensions of the area analyzed was 25 X 25 mm resulting in 10,000 total indents and centered in the midwall location of the weldment. After hardness mapping, the sample was etched to identify the location of the indents in the HAZ with respect to the fusion line.

***Feature cross-weld tests***

Creep specimens machined from the completed weldment had a gauge cross-section of nominally 50 mm (2 inches) through the thickness of the weld, and 15.2 mm (0.60 inches) through the width of the weld, Figure 1. The gauge length was sufficient to include both fusion lines and both HAZs and was nominally 125 mm (5 inches) in length. The gauge length was sufficient to provide metallographic analysis of the failure location as well as damage assessment in the unfailed HAZ. The total area of the gauge cross-section in the feature test samples was ~635 $mm^2$; typical round bar creep specimens have a gauge cross sectional area of 30 to 80 $mm^2$.

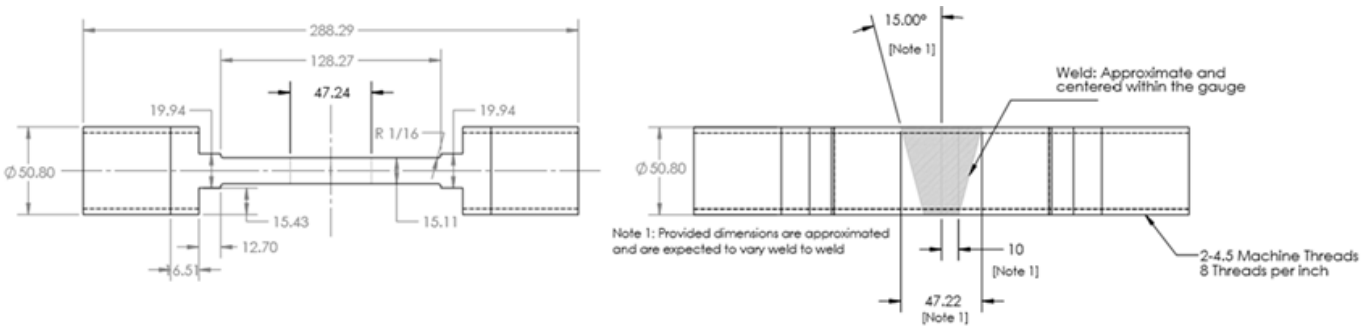


*Figure 1: Feature Cross-weld Test Geometry*

Testing was conducted using constant load machines under a set of standard test conditions for an applied temperature 625°C (1157°F) and stress of 60 MPa (8.7 ksi). These test parameters were selected to result in a HAZ-dominated failures. Three thermocouples were distributed along the gauge length to monitor the temperature. The central 'hot zone' where the test temperature was recorded was within ± 2°C over a length in the gauge of 125 mm. Samples were terminated at a life fraction very close to rupture. For samples which did not completely rupture, testing was terminated upon indication of tertiary creep as the strain was continuously monitored during testing.

***Macro Damage Evaluation***

After termination of the creep test, a macro and micro sample was removed from the sample using fine wire, electrostatic discharge machining (EDM), Figure 2. A Keyence VK-105 confocal laser microscope and a 20X objective was utilized to collect images in the damaged portion of the post-test HAZ. The selected objective provides a collection size for each image of 695 X 522 µm (note that a standard resolution of 1024 X 768 pixels was used). Based on the collection parameters, theoretical minimum cavity size that can be analyzed is 0.70 µm (1 pixel) in diameter. Due to the need for data filtering, the use of the stated 20X objective provides a more realistic analysis of the data where the minimum cavity size is on the order of ~3.5 µm (5 pixels) in diameter.

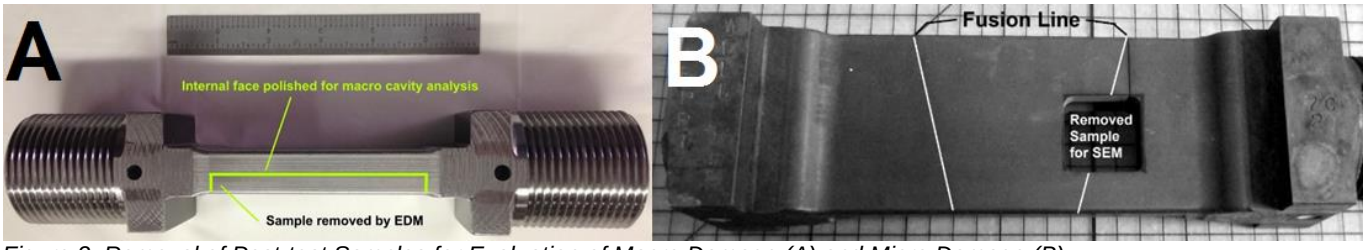


*Figure 2: Removal of Post-test Samples for Evaluation of Macro Damage (A) and Micro Damage (B)*

A total of 270 images (6 images through the width of the HAZ and 45 images through the thickness) were collected for each failed creep test sample. To reduce the number of required images, prior to data collection the sample was rotated such that the 15° bevel created by the machined groove was adjusted to 0°. Accurate spatial position was maintained by an automated stage that has a maximum travel distance of 100 mm in the X and Y orientations.

***Micro Damage Evaluation***

A region measuring approximately 25 X 25 mm was removed (Figure 2B) from the midwall location in both the as-fabricated and post-test condition. The samples were subsequently mounted in conducting Bakelite, followed by grinding using 240 to 1200 grit SiC in a resin bond. The polishing process consisted of polishing the samples using on standard cloths with polycrystalline diamond suspensions with particle sizes of 9 µm, 3 µm and 1 µm. In the final step of polishing the samples were polished using a 0.02 µm colloidal silica suspension or a vibromet automated system.

Scanning electron microscopy was performed using a JEOL 7100 field emission gun system (FEG-SEM) in the as-polished condition using the backscatter electron diffraction (BED) imaging, a working distance of ~6 to 9 mm, 10.0 kV accelerating current and multiple magnifications (generally 1000 to 10000X). Backscatter imaging provided basic observations of the damage present in the HAZ in the post-test condition. Energy dispersive x-ray spectroscopy (EDS) maps were collected in the post-test condition where damage was present, using a working distance of ~12 mm and an accelerating voltage of 15 kV to achieve ~100,000 counts per second (cps). Electron back scatter diffraction (EBSD) was used to evaluate the change in the grain structure starting at the fusion line and moving through the width of HAZ into the parent material. Data was collected for the grain size and orientation using an EDAX Hikari camera and in the as-fabricated condition following PWHT. The data was acquired using a step size of 0.20 µm, an accelerating voltage of 20 Kv and an aperture of 50 µm. Maps were acquired with a field of view of 150 X 150 µm at locations the following locations relative to the fusion line; 0.20, 0.40, 0.60, 0.80, 1.0, 1.4, 1.8 and 3.8 mm. The EBSD data in the as-fabricated condition was linked to the distribution of the macro damage.

## Results

The composition and inclusion analysis for the evaluated parent materials is provided in Tables 3 and 4, respectively. The discrepancy in Table 4 regarding the total feature and analyzed inclusions is a result of some features possessing one or a combination of the following: insufficient counts to determine the type of inclusion, elevated counts for potassium or elevated counts for sodium.

The results for hardness mapping are given in Figure 3. Note that with regard to each image, the unaffected parent material is on the left, then the heat affected zone and the deposited weld metal (all results are provided after post weld heat treatment [PWHT]).

A plot of the damage analyzed in the HAZ for samples 7C-2 and RNT-B2-2 are given in Figures 4 and 5, respectively. The region in each plot highlighted in red corresponds with the area in the HAZ to the highest, statistically evaluated region of damage and as explained in more detail in [13]. With respect to the feature cross-weld tests conducted at 625°C and 60 MPa, sample 7C-2 was terminated after 13,201 hours and for sample RNT-B2-2 after 2,596 hours. A representative image in a high damage field in the HAZ for each sample is provided in Figure 6 as an adjusted brightness and contrast image (creep cavitation damage represented by the black features in each image).

| Sample | Al | As | C | Cr | Cu | Mn | Mo | N | Nb | Ni |
|---|---|---|---|---|---|---|---|---|---|---|
| TP1 | 0.040 | 0.0128 | 0.10 | 8.77 | 0.19 | 0.41 | 0.94 | 0.0454 | 0.071 | 0.12 |
| B2 | 0.020 | 0.0042 | 0.10 | 8.30 | 0.05 | 0.40 | 0.94 | 0.0424 | 0.070 | 0.19 |
| **Sample** | **O** | **P** | **S** | **Sb** | **Si** | **Sn** | **Ti** | **V** | **Zr** | |
| TP1 | 0.0043 | 0.009 | 0.010 | 0.0023 | 0.41 | 0.008 | 0.002 | 0.21 | <0.002 | |
| B2 | 0.0018 | 0.012 | 0.002 | 0.00063 | 0.33 | 0.003 | 0.002 | 0.21 | <0.002 | |

*Table 3: Chemical Composition of the Materials Analyzed (values given in weight percent)*

| Sample | Total Features | Inclusions Analyzed | Al-type | S-rich | MnSi-type | Nb-type | Ca-type | Complex Spinel |
|---|---|---|---|---|---|---|---|---|
| TP1 | 916 | 877 | 28.7 | 51.5 | 0.11 | 2.85 | 4.68 | 10.4 |
| B2 | 7,293 | 5,950 | 4.22 | 92.1 | 0.02 | 0.18 | 3.21 | 0.17 |

*Table 4: Inclusion Analysis (values given as percentage of inclusions analyzed for each inclusion type)*

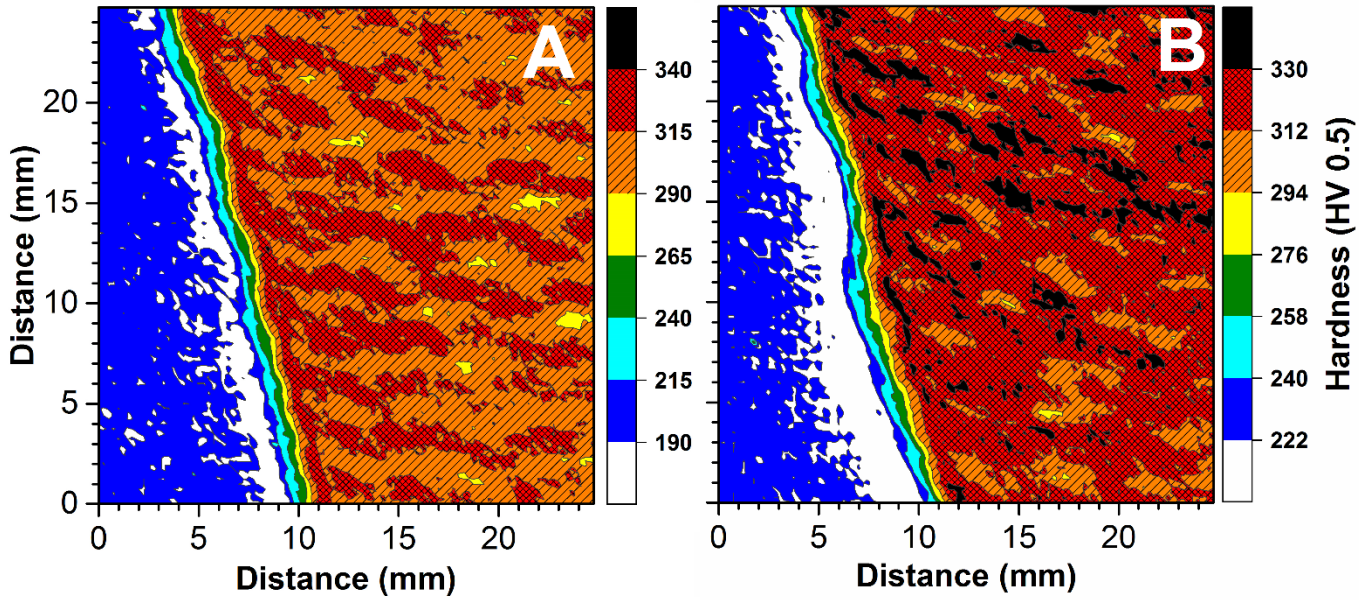


*Figure 3: Hardness Mappings for Weldment in TP1 (A) and RNT-B2 (B); Note that the hardness scales have been adjusted relative to each image.*

A comparison of the hardness map data to the analyzed damage is provided in Figure 7 for sample RNT-B2-2 which exhibited a very high level of damage in the HAZ. Backscatter images for two types of damage are provided for sample RNT-B2-2 in Figures 8 and 9. In Figure 8, damage that is not clearly associated with inclusions and appears to be isolated at grain boundaries are provided. Figure 9 provides a second population of damage which is clearly associated with inclusions. The detail of these inclusions is described in Figure 10 for a set of cavities around Al- and Mn- rich particles.

Figure 11 provides results for the SEM-EBSD analysis in the as-fabricated condition and as linked to the distribution of peak damage in sample RNT-B2-2. Although in each of Figures 7 to 11 the emphasis is on a single sample (RNT-B2-2) a similar set of observations were noted for sample 7C-2.

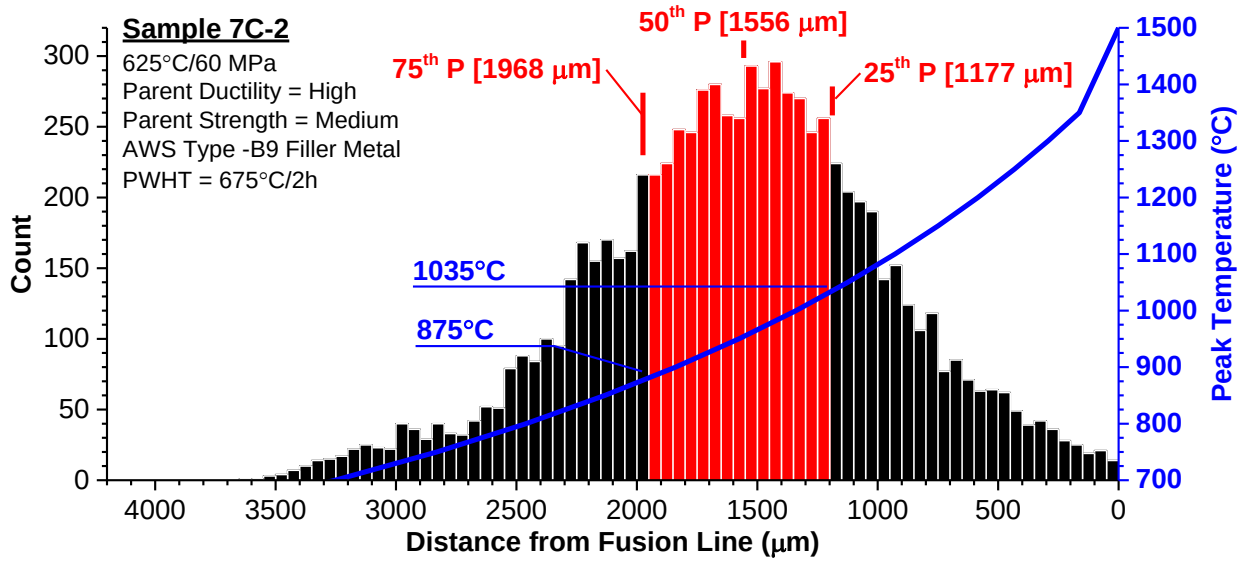


*Figure 4. Distribution of Damage in Sample 7C-2 (parent metal TP1) after Testing at 625°C, 60 MPa and 13,201 hours*

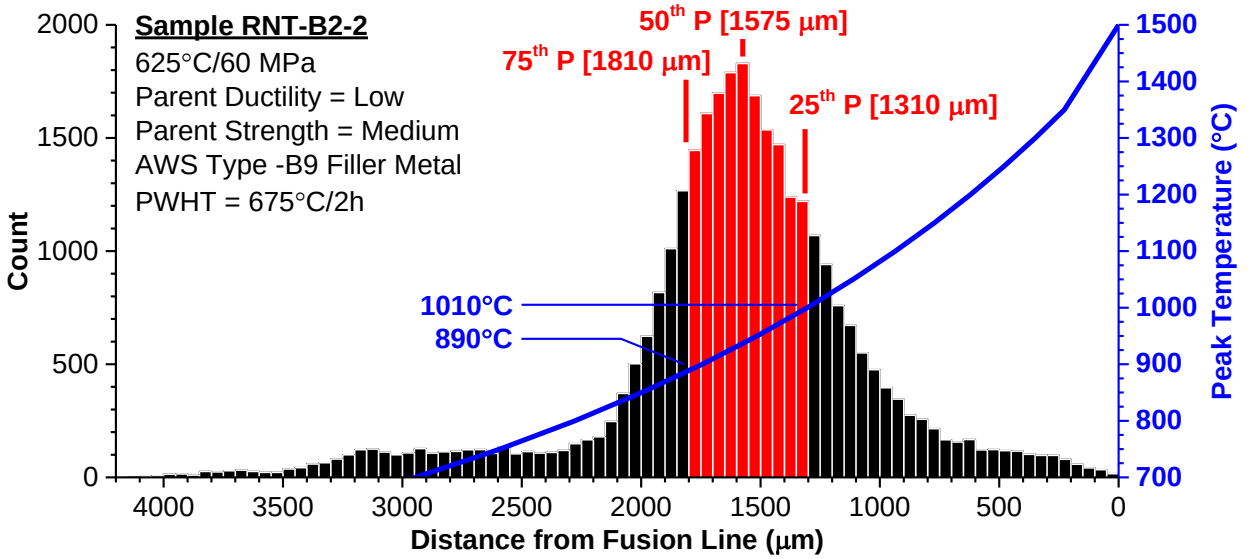


*Figure 5. Distribution of Damage in Sample RNT-B2-2 (parent metal B2) after Testing at 625°C, 60 MPa and 2,596 hours*

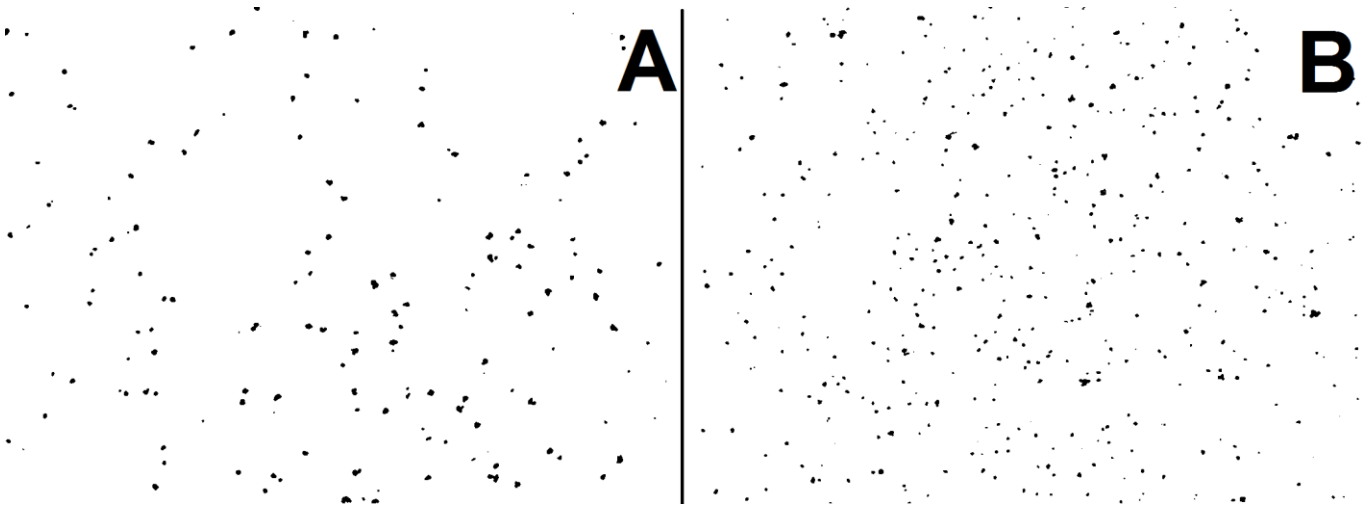


*Figure 6. Creep Damage in the Heat Affected Zone where a High Density of Cavities is Noted, Sample 7C-2 435 voids/mm$^2$ (parent metal TP1) [A] and Sample RNT-B2-2 1,255 voids/mm$^2$ (parent metal B2) [B]*

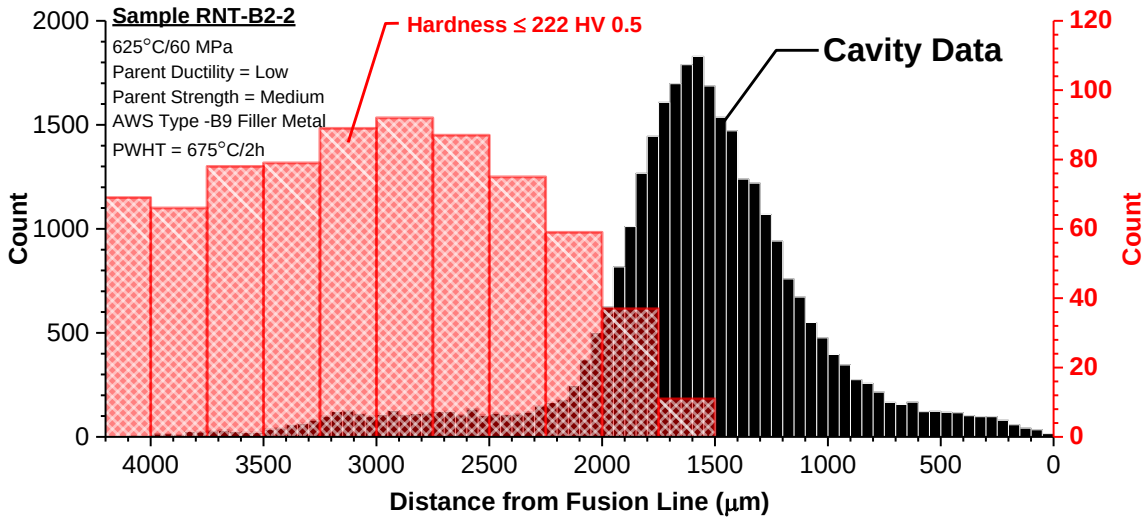


*Figure 7. Comparison of the Hardness Data in the Low Hardness Region (Red Histogram) to the Distribution of Damage (Black Histogram) for Sample RNT-B2-2 (parent metal B2). Note that the distribution of hardness indents ≤222 HV 0.5 are identified in Figure 3B by the white region in the HAZ*

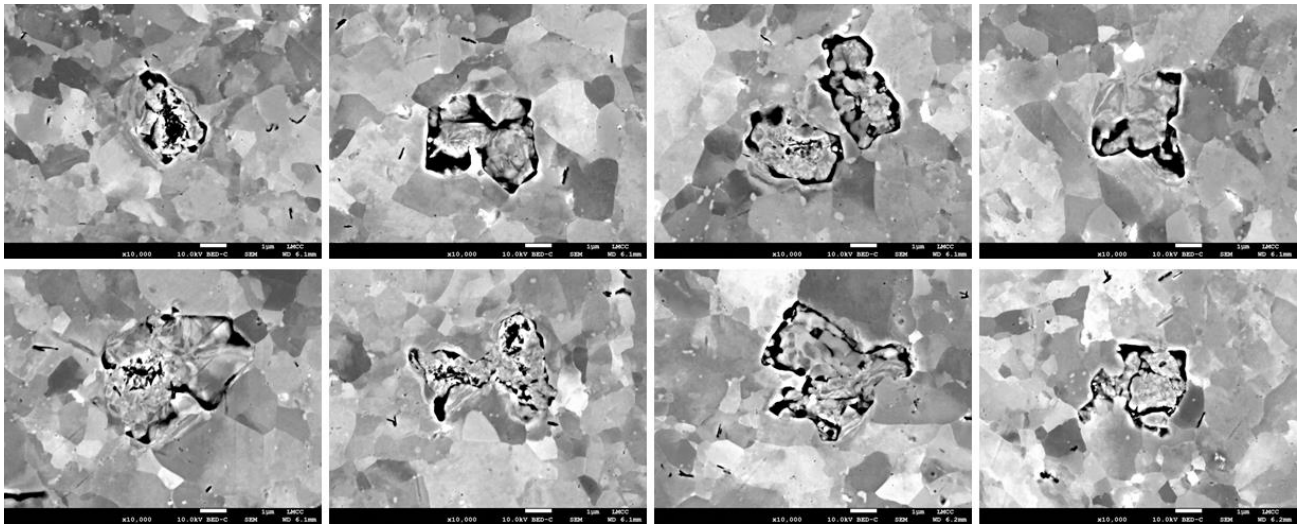

*Figure 8. SEM Backscatter Images of Creep Cavities which appear to be isolated to Grain Boundary Features in the Heat Affected Zone in Sample RNT-B2-2 (parent Metal B2), Note all images at 10,000X magnification*

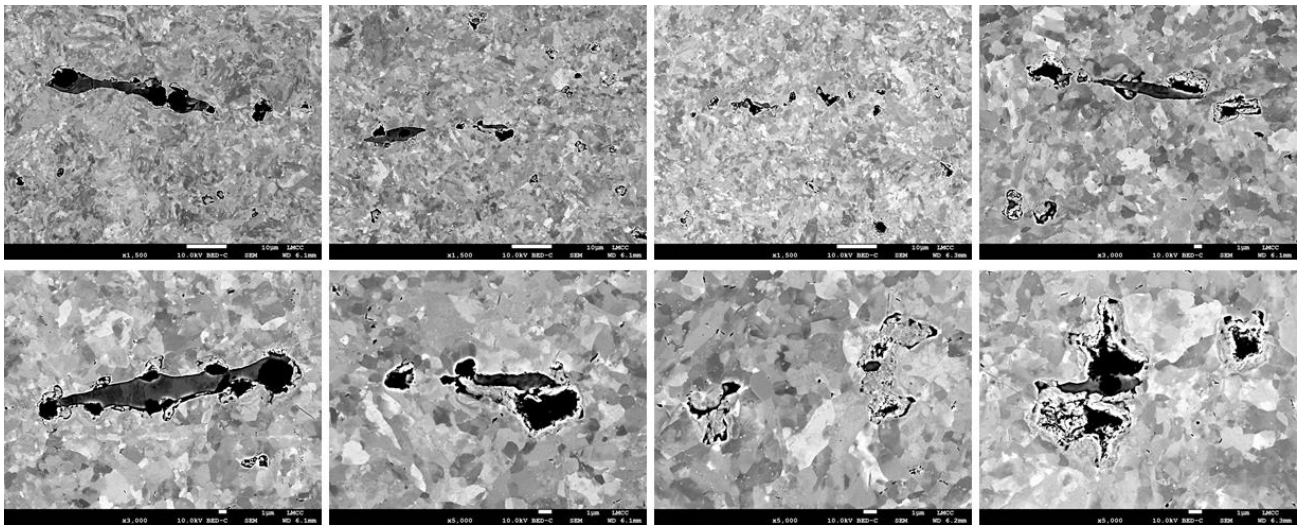

*Figure 9. SEM Backscatter Images of Creep Cavities which are Associated with Inclusions in the Heat Affected Zone in Sample RNT-B2-2 (parent Metal B2), Note variable magnification in each image*

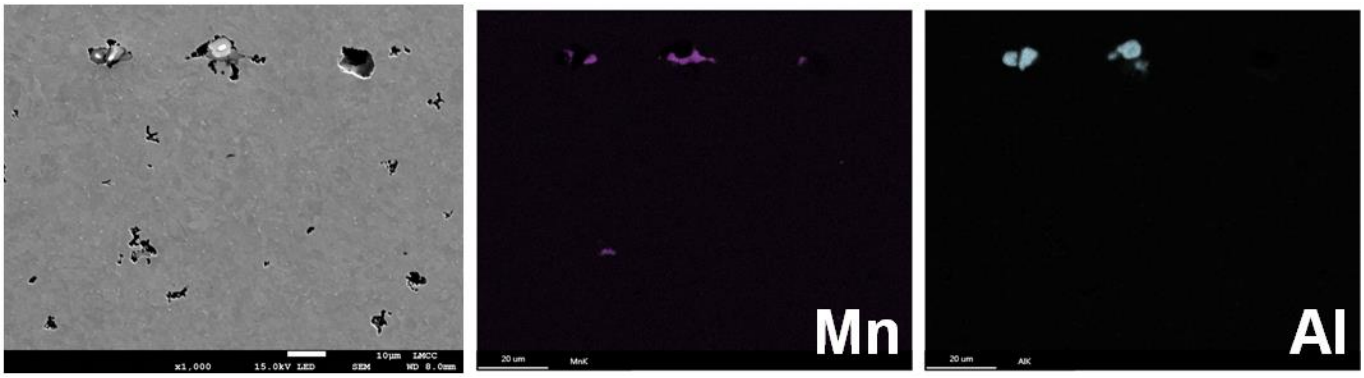


*Figure 10. SEM-EDS Analysis for Damage at Inclusions in Sample RNT-B2-2 (parent Metal B2) and for Al and Mn*

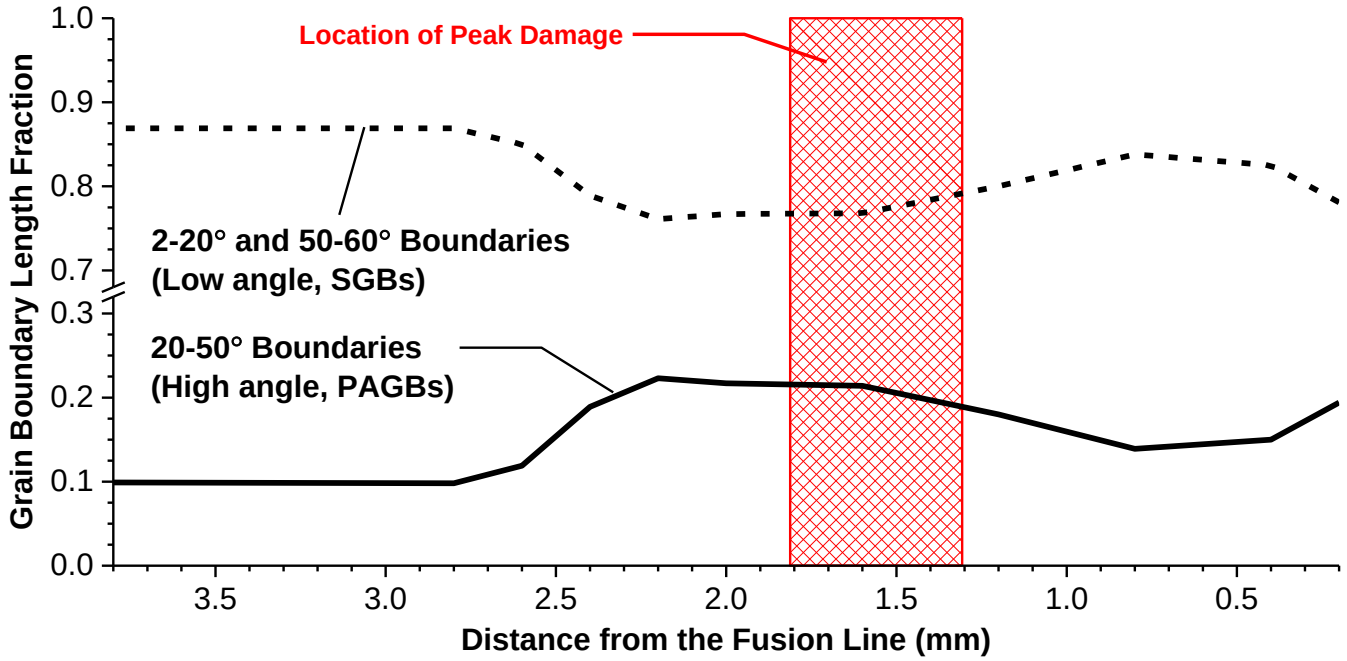


*Figure 11. SEM-EBSD Analysis of Low and High Angle Grain Boundary Distribution through the Width of the HAZ and as Linked to the Distribution of Peak Damage in Sample RNT-B2-2 (parent Metal B2)*

## Discussion

There is a notable difference in cross-weld creep performance in the evaluated parent materials. The life reduction of ~5X for an identical cross-weld creep test condition is not reflected in the measured, parent metal creep strength. As both materials achieved a similar creep life when evaluated prior to welding, the contribution of damage (as manifested by the large difference in creep ductility) must be considered. The overall extent and amount of damage present in the HAZ for the poor ductility B2 sample was ~3X higher on the basis of analysis in an individual image comparison, such as that provided in Figure 6 and ~5X higher for the measured peak damage in Figures 4 and 5. Factors which are believed to contribute to this dramatic difference are explained in the subsequent summary.

Damage is often identified with an over-tempered region in the HAZ, e.g. such as the white region identified in Figure 3. However, and consistently for numerous samples including data not presented here, there is consistent association of peak damage and failure in the HAZ region adjacent to this over-tempered region and as exemplified in Figure 7. In the HAZ then there is must exist subtle details in the microstructural zones with respect to deformation and damage. This situation is exacerbated, e.g. the tendency to damage-dominated failures, by the feature test cross-sectional area which results in a multiaxial stress state. The multiaxial stress state results in high triaxiality and enhances the evolution of damage in a process analogous to in-service component behavior. It is important to note that damage observations made in the HAZ for small, round bar samples more typical of cross-weld creep evaluations in the literature may not result in the same conclusion presented here as the sample geometry (e.g. that damage and failure occur adjacent to the over-tempered zone and not in this zone). Small samples with gauge diameters conventionally on the order of <6.5 mm are insufficient to induce a sustained triaxial stress state through the thickness of the HAZ.

A direct comparison of the damage present in the HAZ for the analyzed cross-weld samples is provided in Figure 12 shows that the damage in the RNT-B2-2 sample is dramatically higher than that for the 7C-2 sample. Evaluation of damage in the HAZ in Figures 8 and 9 suggests that two populations of damage exist in the HAZ; one set with grain boundary features and a second set with inclusions/particles in the HAZ. For the population which does not appear to clearly be linked to inclusions, it is important to note that the reliance of the provided observations are 2D, e.g. there may or may not be an inclusion which exists either below the evaluated plane (and hidden from view) or above the evaluated plane (and removed by polishing).

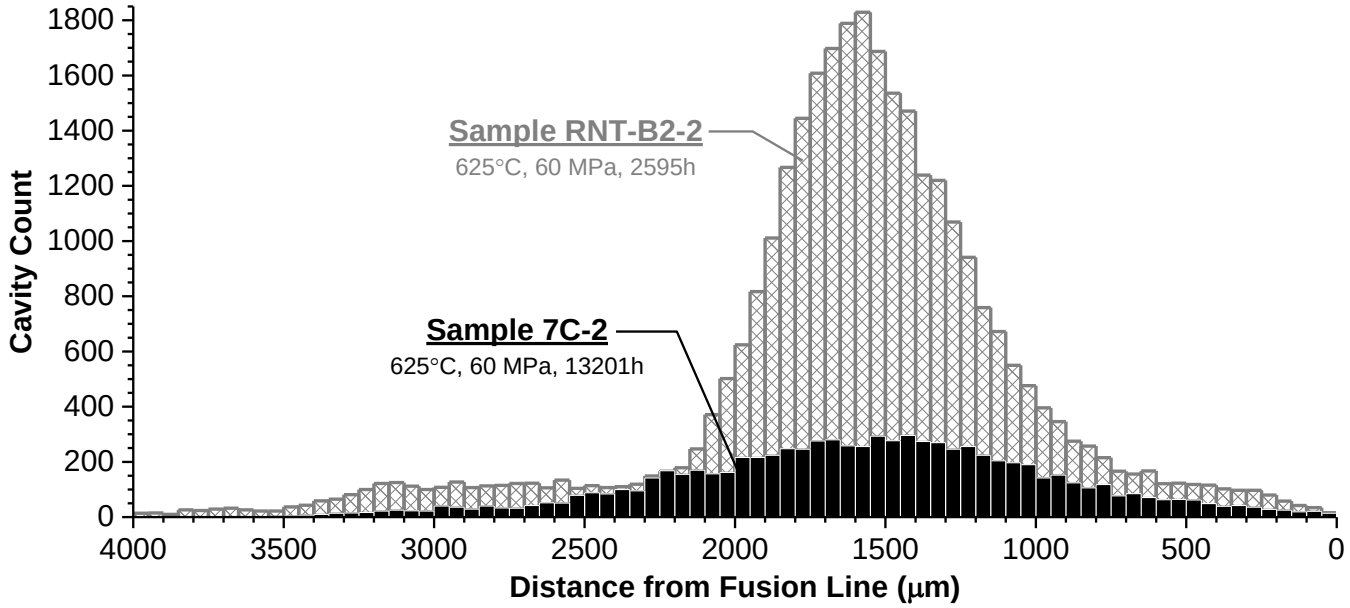


*Figure 12. Comparison of the Damage in the HAZ provided in Figures 4 and 5*

The composition and inclusion content in Tables 3 and 4 at least partially explains the observations in Figure 12. There is a markedly higher content of tramp elements in the B2 material evaluated in test RNT-B2-2 as well as a population of inclusions which is ~10X high than that for the TP1 material (sample 7C-2). The density of analyzed inclusions in sample RNT-B2-2 (~150/mm$^2$) cannot alone account for maximum distribution of damage which is measured at >1,000 voids/mm$^2$, Figure 6. It should be noted that the inclusion analysis is limited to the physics of the process, e.g. the EDS spot size which is ~1 µm in diameter and it may be rationalized that some inclusions are unable to be properly accounted for in the analysis.

Despite the physical limitations of the inclusion analysis, there is clear evidence that the damage observed in the HAZ more closely trends with the inclusion density than to other identified phases which have been suggested to be linked to damage in 9%Cr steels. The measured density (given in /mm$^2$) for $M_{23}C_6$ is measured in the 1,000,000s of particles, for Laves phase by the 100,000s of particles, for AlN by the 10,000s of particles and for inclusions by the 100s of particles. As both heats of material exhibit considerable AlN (as expected by the relatively low N:Al ratio of 2 for TP1 and 1 for B2 material) an additional contribution of AlN to the present damage in the HAZ may be a reasonable claim. This and additional features in the HAZ are under investigation to more completely understand and explain association of the damage present in the HAZ to particles and features.

Analysis of the compositions provided in Table 3 and under equilibrium conditions on-cooling from melting is provided in Figure 13. In this Figure only the primary elements in the specification were considered: Al, C, Cr, Fe, Mn, Mo, N, Nb, Ni, P, S, Si, V using the ThermoCalc database TCFe7 Steels/Fe-Alloys v7.0 and for the liquid, MnS and AlN phases. The influence of composition on the formation of MnS and AlN for the two evaluated heats of material is dramatically different. With regard to the B2 material (identified as 'Barrel 2' in the figure), there is a larger mass fraction of both MnS and AlN as well as increased stability of these phases. The influence of poor composition in B2 is compounded by the overlap of the liquid phase with the formation of MnS, suggesting that the simultaneous evolution of MnS with the liquid would result in the MnS acting as an ideal trap site for low melting point constituents. The melting temperature for elements such as As, Cu, Sb and Sn is well below that of the matrix and the solidification behavior of the material may promote the concentration of these tramp elements to particles which form at solidification such as MnS. As the grain size in the HAZ is typically ~1 to 5 µm and is therefore generally the same

size as MnS, the MnS will intersect newly formed grain boundaries in the HAZ and may result in elemental segregation along grain boundaries. Whether tramp elements reside at MnS or on grain boundaries, the local surface energy at these interfaces will be reduced and result in a reduction in the stress required for nucleation [14]. The presence of a particle in these locations (e.g. inclusions) can cause an enhancement of the stress and intensify strain. Support for this phenomenon is given in Figure 14 where a region above and below the MnS inclusion is apparently recrystallized.

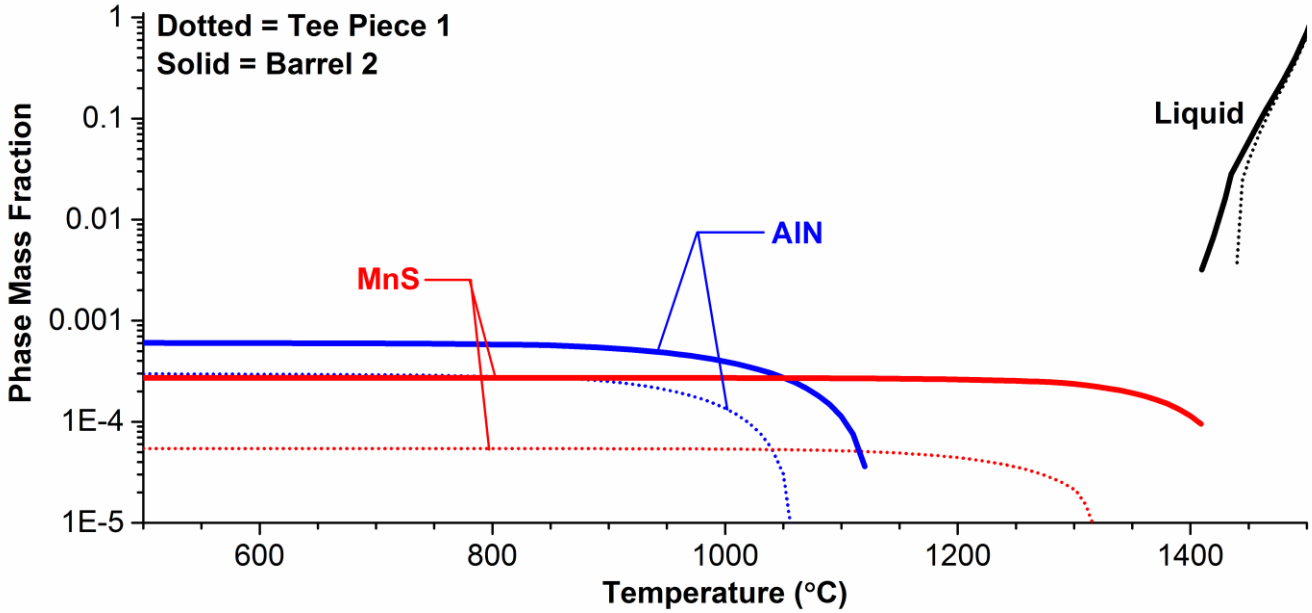


*Figure 13: Equilibrium Simulation for Materials B2 and TP1 (Table 3) and for the Liquid, MnS and AlN phases*

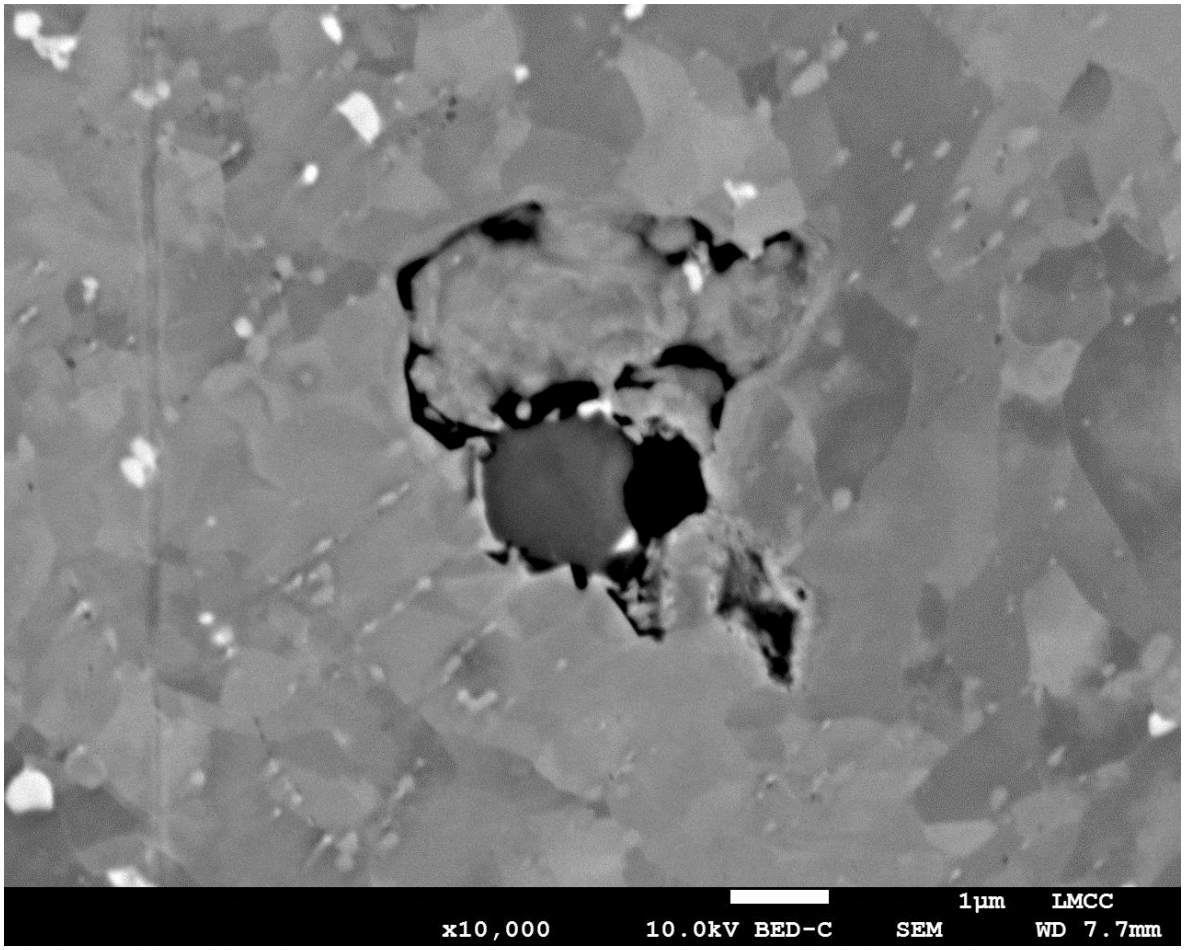


*Figure 14: Recrystallization at a MnS Particle in the Heat Affected Zone*

The contribution of the HAZ grain structure to the evolution of damage is detailed in Figure 11. The overlap of maximum, peak damage to a local increase in the HAZ for grain boundaries with a misorientation of 20 to 50 degrees is well-explained by the temperature distribution in Figure 5. In the location of the HAZ where damage is identified, there is a compounding effect from the peak temperatures which are below the conventional minimum normalization temperature for Grade 91 steel of 1040°C. For the stated temperatures where damage is noted, e.g. ~875 to 1035°C and for the non-equilibrium heating and cooling the HAZ material is expected to be highly non-homogeneous. Although the poor grain structure in the HAZ contributes to poor performance in cross-weld samples for 9%Cr steels, the effect is similar for both parent materials evaluated in this study, e.g. both weldments were fabricated with similar procedures (Table 2). Thus the heterogeneous grain structure cannot on its own account for the poor performance observed in the RNT-B2-2 sample as compared to the 7C-2 sample (e.g. failure times in cross-weld creep of 2,596 versus 13,201 hours, respectively).

## Conclusion

The evaluation of damage in the HAZ of two Grade 91 steel feature cross-weld samples provided a number of relevant observations detailed below:

1. Failure in cross-weld creep samples occurs in a location adjacent to an over-tempered softened region in the HAZ and not in the location of lowest hardness;
2. There is a notable contribution of composition, including the content of tramp elements (e.g. As, Cu, Sb, Sn) and inclusion content on cross-weld creep performance. The impact of these elements in the pre-welded condition was noted by a large difference in creep ductility measured as reduction of area in the parent materials;
3. Two populations of creep cavities in the HAZ exist. There are cavities which exist primarily at grain boundary features with no apparent association with an inclusion or particle (although the reported information relies on 2D evaluation). The second population of cavities exist at inclusions resulting from steel-making and are predominately associated with S-rich (e.g. MnS type) and Al-rich (e.g. Alumina-type) inclusions.
4. Damage was concentrated in a region in the HAZ corresponding with a calculated peak temperature in the range of 875 to 1035°C and in a location where EBSD identified a higher area fraction of high angle grain boundaries.

The contribution of factors which affect damage evolution in the HAZ of 9%Cr steels cannot be minimized. The evaluation of the parent materials in this study included two materials which exhibited nearly identical creep lives but when tested in cross-weld creep using large, feature type samples showed considerable difference in cross-weld creep performance (e.g. a factor of 5X). The vast difference in creep ductility in the parent material, e.g. 15 versus 83% in reduction of area is explained by a higher inclusion density and poor composition in the poor ductility material. These features contribute to the poor cross-weld creep performance and highlight a need for researchers to more carefully consider factors which contribute to damage in 9%Cr steels resulting in poor performance in welded structures.

## Abbreviations

| | |
|---|---|
| HAZ | Heat affected Zone |
| PWHT | Post weld heat treatment |
| CSEF | Creep strength enhanced ferritic |
| SEM | Scanning electron microscopy |
| BED | Backscatter electron diffraction |
| EDS | Energy dispersive x-ray spectroscopy |
| EBSD | Electron backscatter diffraction |
| MnS | Manganese sulfide |
| AlN | Aluminum nitride |

## References

[1] *Service Experience with Grade 91 Components*. EPRI, Palo Alto, CA: 2009. 1018151.
[2] *Service Experience with CSEF Steels in Power Plants in the Asia-Pacific Region.* EPRI, Palo Alto, CA: 2015. 3002005089.
[3] S. J. Brett, D. J. Allen and J. Pacey. "Failure of a Modified 9Cr Header Endplate." in *Proceedings of an International Symposium on Case Histories on Integrity and Failures in Industry*, Milan, Italy, 1999.
[4] S. J. Brett and J. D. Parker. "Creep Performance of a Grade 91 Header." *International Journal of Pressure Vessels and Piping* 111-112, 2013. pp. 82 to 88.

[5] A. Nitsche, D. Allen and P. Mayr. "Damage Assessment of Creep Affected Weldments of a Grade 91 Header Component after Long-term High Temperature Service." *Welding in the World* 59 (4), 2015. pp. 675 to 682.
[6] M. Gold, J. Hainsworth and J. M. Tanzosh. “Service Experience with Design and Manufacturing Approaches with T/P91 Materials.” *EPRI Conference on 9Cr Materials Fabrication and Joining Technologies*. EPRI, Palo Alto, CA: 2001. 1006299. pp. 15-1 to 15-20.
[7] M. Rauch, K. Maile, P. Seliger and A. Reuter. “Creep damage development in martensitic 9Cr steels.” *VGB PowerTech*, September 2004. pp. 71 to 75.
[8] *NDE Methods for Detection of High Temperature Damage in CSEF Steels Grades 91 and 92 as a Basis for Life Evaluation*. EPRI, Palo Alto, CA: 2015. 302005187.
[9] J. D. Parker, K. Coleman, J. A. Siefert and J. P. Shingledecker. "Challenges with NDE and Weld Repair of Creep-Strength Enhanced Ferritic Steels." *Advanced Materials & Processes* 170, 2012. pp. 20 to 23.
[10] D. J. Kotecki. “Fourth Round Robin Report – Trace Elements in Cr-Mo-V Steel Weld Metal.” *Welding in the World* 60 (4), 2016. pp. 639 to 643.
[11] *A Perspective on the Selection of Preheat, Interpass and Post-weld Cool Temperatures Using Grade 91 Steel as an Example*. EPRI, Palo Alto, CA: 2015. 3002005351.
[12] O. Grong. *Metallurgical Modelling of Welding, 2nd Edition*. Editor H. K. D. H. Bhadeshia. The Institute of Materials, Cambridge, UK: 1997. pp. 3, 35, 40.
[13] J. D. Parker and J. A. Siefert. “Evaluation of the Creep Cavitation Behavior in Grade 91 Steels.” *International Journal of Pressure Vessels and Piping* 138 (2), 2016. pp. 31 to 44.
[14] H. Riedel. *Fracture at High Temperatures*. Springer-Verlag, Berlin: 1987. pp. 129.